Four-point bending test on a middle strength rock: numerical and experimental investigations

Aria Mardalizad, Riccardo Scazzosi, Andrea Manes, Marco Giglio
Politecnico di Milano, Department of Mechanical Engineering, Via La Masa 1, 20156 Milan, Italy
aria.mardalizad@polimi.it, riccardo.scazzosi@polimi.it, andrea.manes@polimi.it, marco.giglio@polimi.it

ABSTRACT. Developing a reliable numerical modelling technique is considered as challenge for fracture assessment of the geological materials, which are much subjected to hydrostatic pressure. For this purpose, the mechanical behaviour and the fracture pattern of a middle strength rock material, called Pietra Serena sandstone, is investigated both numerically and experimentally under a Four-Point Bending (also called Flexural) testing program. For the numerical approach, an innovative method, namely FEM-coupled to-SPH, is exploited due to its capabilities in dealing with rock mechanics related issues. Two different material models, which are the Karagozian and Case Concrete (KCC) and the Extended (Linear) Drucker-Prager, are exerted to assess their capabilities. The Flexural strength and the crack initiation area are studied based on the state of the stress in various parts of the specimen in both models, and finally the results obtained from the numerical models are compared with the data obtained from the experimental tests in order to assess the capability of the modelling approach.

KEYWORDS. Flexural test; KCC; Dracker-Prager; Pietra Serena; Fracture.

INTRODUCTION

Rock materials are highly dependent on the hydrostatic loading pressure, moreover their tensile strength is considerably weaker than the compressive one. Thus, the characterization of the tensile behaviour is of great importance in geophysical applications. The tensile behaviour of rock materials, which is also one of the most important parameters to predict the rock's boreability, can be determined in several ways, i.e. by a direct tensile test, a Brazilian splitting disk test, a (three- or four- point) bending test, etc [1]. The direct tensile test seems to be the standard way to determine the maximum principal tensile strength of rock materials. However, due to several issues, including the complicated set up, the non-uniformity and the perturbation in the uniaxial stress field introduced by specimen grips and/or slight imperfections in the sample preparation and the material inhomogeneity, etc., its usage is inconvenient [2-4]. Therefore, rock engineers perform the Brazilian and the Flexural (four-point bending) test to investigate the tensile behaviour. These tests are designed to investigate indirectly a normal tensile stress state (at least) in a specific portion of the specimen. The numerical and experimental investigation of the mechanical behaviour of a middle strength rock material which is subjected to a Four-Point Bending (or Flexural) test is the aim of this research study.

The Four-Point Bending test is an indirect way to estimate the tensile strength, which consists of a beam in flexure. The strength of the beam, in this test, is expressed mainly in terms of modulus of rupture, which usually tends to overestimate the tensile strength up to one-hundred percent [4]. This overestimation is mainly caused by the hypothesis of the test which

assumes that the mechanical characteristics, i.e. the stress-strain behaviour, are linear all the way through the critical cross-sectional area of the beam [5]. Due to the sensitivity of this test to the boundary conditions, it may be inaccurate in large displacement (which is similar to the direct tensile test) [6]. In addition to these difficulties, the strength of quasi-brittle materials, e.g. rock, is considered to be dependent on their size and scale [7-9]. However, the Flexural test is considered as the simplest method to investigate the creep (time-dependent behaviour) of rock [10], and accordingly, represents an interesting alternative for the investigation of the stress-strain relationships [11, 12]. The experimental campaign designed for this research study follows the protocols of the ASTM standard and the results can therefore be easily compared with similar studies, i.e. on other materials.

The mechanical properties of several types of rock materials, including sandstones have been studied in a large variety of research. Among them, the Berea sandstone which is deposited sub-aqueously as offshore beds in a considerable number of well drilling applications, is widely investigated by the oil and gas industries [13, 14]. It is a sedimentary rock with high porosity and mostly composed of sand-sized grains [15], however, it is not a highly accessible material resulting in a relatively high expense for testing purposes. An extensive literature review [16-18] exposed the presence of another rock material, which is called Pietra Serena sandstone, with similar mechanical characteristics to Berea sandstone. These similar properties led the authors to perform the experimental tests on the Pietra Serena sandstone. It is anticipated that the experimental data of the flexural test on the Pietra Serena can be used to have an outlook of the behaviour of Berea sandstone.

The development of a reliable numerical method in conjunction with an accurate constitutive material model has been considered an essential tool in the stress analyses. Several numerical modelling techniques have been recently implemented [19-23] to simulate the rock materials. One of the most common and accurate numerical simulation techniques, which is implemented in research fields as well as in industrial applications, is the Lagrangian Finite Element Method (FEM). However, this method cannot appropriately deal with large deformations and tearing, which are often present in the numerical modelling of fractured rock. The Smooth Particles Hydrodynamics (SPH), on the other hand, is a mesh-free Lagrangian method that discretizes a system into a number of "mesh-points" (or particles) carrying the field variables. Due to the not fixed nodal connectivity of this method, the SPH is able to cope with highly distorted elements [21, 24, 25]. The FEM is however more efficient in terms of accuracy and computation time when SPH particles are used. Therefore, an advanced technique is exploited, inspired by the research study of the same authors of the present paper, Bresciani et al., [25] to take advantage of both the Lagrangian FEM (before the occurrence of high distortion) and the SPH methods to deal with large deformation, mesh distortion, etc. In this numerical model, which is called FEM-coupled to-SPH, the specimen is initially modelled by Lagrangian 3D elements and subsequently by means of an eroding algorithm. The elements which reach a specific failure level are eroded, and subsequently these eroded elements are transformed to SPH particles with the same mechanical properties.

Two commercial numerical solvers, LS-DYNA and ABAQUS, are used to replicate the experimental tests in conjunction with two constitutive material models: the Karagozian and Case Concrete (KCC) model and the Extended (Linear) Drucker-Prager (LDP) model. The KCC is an advanced material model, developed by Malvar et al. [26-29], available in LS-DYNA, that decouples the volumetric and deviatoric responses. This material model consists of three-independent failure surfaces to determine the accumulated damage. The LDP, on the other hand, is based on the conventional Drucker-Prager model. This material model which is available in ABAQUS, takes advantage of some improvements, i.e. the flow rule plasticity [30] and is particularly interesting due to the potential use of different shapes of the yield function (linear, hyperbolic and exponential), and additional cap yield function and the possibility to be used in conjunction with an equation of state. However, due to the lack of a tension (or pressure) cut-off level, the numerical results have to be critically evaluated. The numerical results of the KCC and LDP are thus compared in detail to show the reliability of the models.

The article is divided into the following sections. The methods and the results obtained during the experimental tests are reported in section 2. In section 3, the theories of the KCC and the LDP material models are discussed in detail. Then the experimental configuration suggested by the ASTM is replicated in LS-DYNA and ABAQUS by the FEM-coupled to-SPH method in conjunction with the KCC and the LDP material models, respectively. The numerical results of these models are then compared with each other and discussed in section 4 by the further comparison of the numerical modelling results with the experimental data.

EXPERIMENTAL TEST

The experimental configuration for the Flexural test is designed based on the protocols of the ASTM standard [31]. This configuration consists of a rectangular cubic specimen which is supported by two fixed rollers near the end of its length span (see Fig. 1a). Thus, the specimen is loaded vertically by means of two compressive rollers at a certain

distance from the center of the specimen. This symmetrical configuration causes nominally zero shear forces, and accordingly constant bending moment between the two compressive rollers. The normal tensile and compressive stresses appear at the top and bottom of this middle span, respectively. According to the beam theory, the maximum principal stress corresponding to the ultimate loading value can be determined, which is called the flexural strength and gives a rough approximation of the principal tensile strength.

The flexural strength tends to overestimate the tensile strength, because the measuring process considers a linear relationship (as the stress-strain behaviour of the material) at the beam critical cross-section. Furthermore, all the materials have a certain amount of anisotropic level in their structure [4]. The flexural strength $\sigma_{flex.}$ [MPa], which is given by the Eq. (1), can be considered as a parameter to validate the numerical models.

$$\sigma_{flex.} = \frac{3WL}{4bd^2} \tag{1}$$

where, W was measured as the maximum applied force. The experimental tests within this study were performed on five specimens of Pietra Serena sandstone with the same geometries. The span length L, width b and height d of all the specimens were equal to 318, 102 and 32 [mm], respectively. However, the total length of the specimen was measured as 381 [mm]. Two pairs of steel rods were embedded to the testing apparatus (see Fig. 1). The axes of lower rods were fixed to the bed of testing machine while the upper rods were displacement controlled by means of a compressive platen. According to [31] the speed was set to 0.2 [mm/min] in order to apply the load at a uniform stress rate of 4.14 [MPa/min].
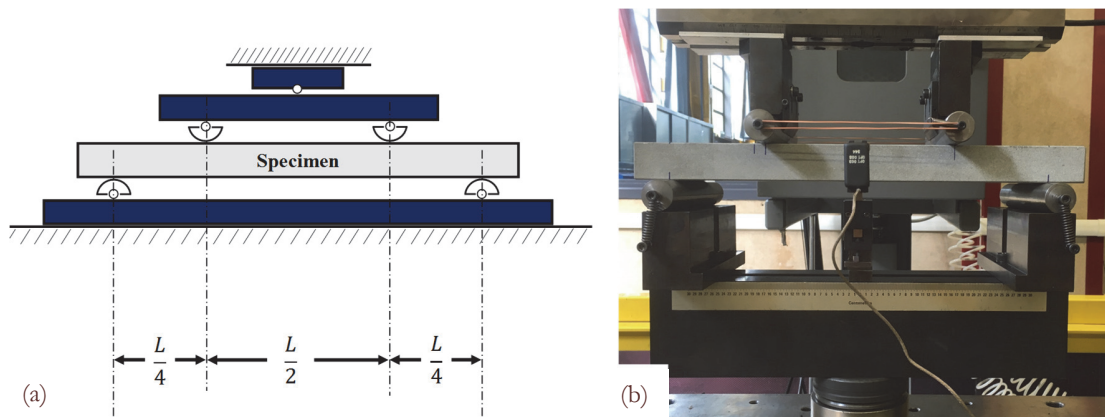

Figure 1: (a) ASTM arrangement of Flexural test [31]; (b) corresponding experimental layout of this research work.
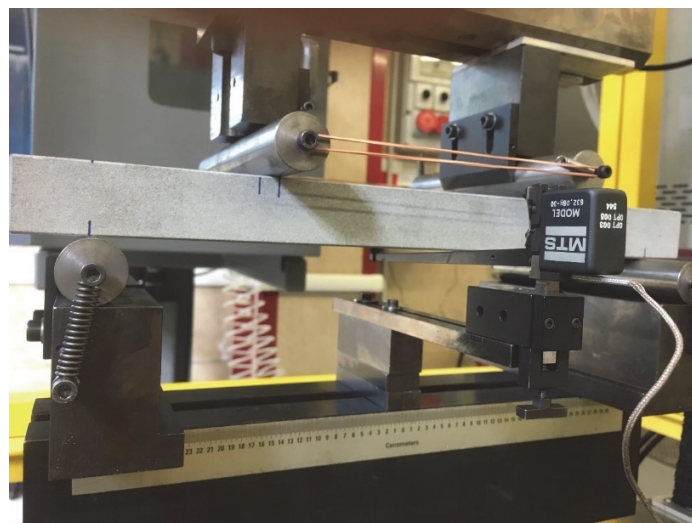

Figure 2: The extensometer set up on the flexural test configuration.

This study is aimed to investigate the mechanical response of the rock based on both the maximum loading and the displacement. The applied load of the compressive platen was measured automatically by the load cell of the apparatus. It is not mentioned how to measure the displacement of the specimen on the ASTM standard. It was decided to measure the displacement of the specimen by means of a displacement gage contacting extensometer. As can be seen in Fig. 2, the flexible tip of the extensometer is located at the center of the lower face of specimen. However, since the extensometer, itself, is fixed to the fixture of the testing machine, the displacements of all the components in between are measured. Therefore, in the configuration expressed in Fig. 2, the experimental data provided by the extensometer contains the displacements of the specimen, the fixed rollers and the steel blocks between the rollers and the fixture of the apparatus. This set of data therefore doesn't represent the actual displacement of the specimen, but since the mechanical properties of the rollers and the steel blocks are known, they can be replicated in the numerical simulations as well. This set up is thus a convenient way to record the experimental data of the flexural test in terms of displacement.

The broken specimens after performing the flexural test are indicated in Fig. 3. In all of the specimens, cracks initiate at the lower part, which is subjected to tension stresses and then propagate in an upward manner through the depth. Also, the cracks are located under (and close to) the section of the specimens which are in contact with the moving rods.
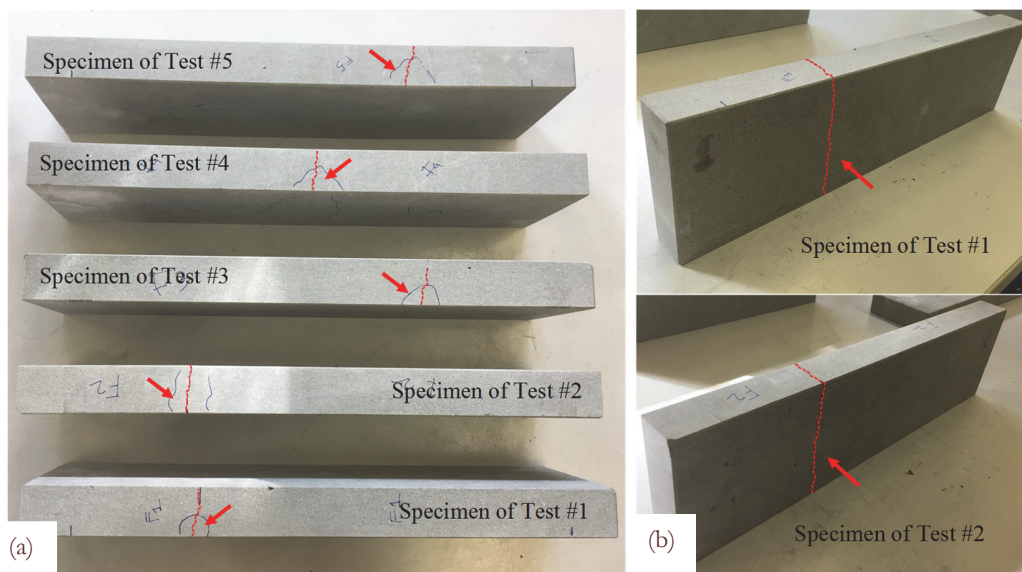

Figure 3: The broken specimens after performing the flexural test; (a) front view; (b) isometric view.

The maximum load, displacement and the flexural strength are reported in Tab. 1, separately for each specimen. Average values, 95% Confidence Interval ("95% CI") of the average value and standard deviations has been also calculated from experimental data. CI is an interval that try to estimate range of the average value of the population from the sample data. Due to the large variability of the mechanical behavior of rock this range is more representative than the single average value obtained from the 5 experimental tests. Fig. 4 also expresses the load-mid span displacement diagram of the all specimens.

	Maximum Load [kN]	Maximum displacement	Flexural Strength [MPa]
Specimen K1	3.59	0.502	8.3124
Specimen K2	4.258	0.662	10.024
Specimen K3	2.963	0.313	6.831
Specimen K4	4.16	0.669	9.7927
Specimen K5	4.206	0.628	9.9576
Average value	3.8354	0.5548	8.9836
"95% CI" of average value	[3.1433; 4.5275]	[0.36737; 0.74223]	[7.2530; 10.7140]
Standard deviation	0.55736	0.15095	1.3937

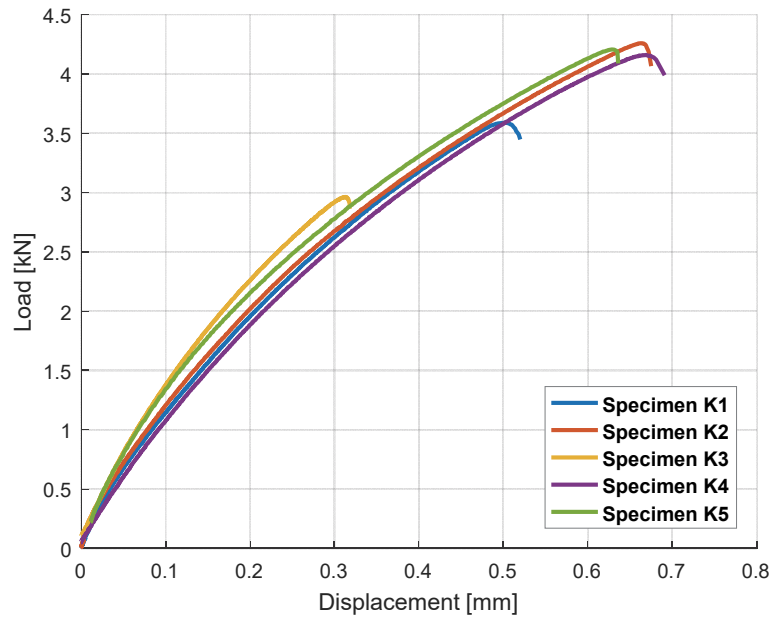Table 1: The experimental results of the flexural test.

Figure 4: The load-displacement diagram of the flexural test.

The shape of the load-mid span displacement, represented in Fig. 4, indicates a significant non-linear behaviour until the failure. The failure is denoted by a sudden drop of the loading level. A study by Meda et al. [32], investigated Pietra-Serena sandstone under a flexural test. They performed the tests on specimens with different shapes and considered a notch in the middle-span of the specimens to assure that the crack takes place at the center. The experimental data provided by Meda et al. are in a good agreement with the results obtained during this research work where the geometries are similar to each other; i.e. the flexural strength and the load-displacement diagrams of the Meda's work were reported as 9.1 MPa and 3.4 mm, respectively.

NUMERICAL MODELLING

Many numerical modelling techniques have been developed for stress analyses of solid mechanics in the continuum domain. Among these, the non-linear Lagrangian Finite Element Method has its own privileges for a number of reasons, i.e. the accuracy and the convenient time consumption cost. However, a disadvantage lies within the reduced performance of grid-based numerical methods to deal with highly distorted elements and fragmentation. At present, the Smooth Particle Hydrodynamics (SPH) is one of the most convenient numerical methods to cope with problems related to large deformations and fracture. This method is a numerical mesh-free approach that represents the state of a system by a set of particles that hold the properties of the material. The particles interact in a range which is controlled by a kernel (smoothing) function, so that this kernel approximation for any two given particles, *i* and *j*, can be expressed by Eq. (2).

$$f(x_i) = \int_{\Omega} f(x_j)W(x_i - x_j, h)dx_j \qquad (2)$$

where, the *W* in Eq. (2) is the smooth function which can be determined by Eq. (3).

$$W(x_i - x_j, h) = \frac{1}{h(x_i - x_j)^d}\theta(x_i - x_j) \qquad (3)$$

The x_i and x_j are the coordinates of the particles in the problem domain Ω and *h* is the distance between the two particles. The parameters *d* and θ in Eq. (2) represent the number of the space dimension and an auxiliary function, respectively (see

Fig. 5). Because the connectivity between these particles is considered as a part of the computation procedure, a straightforward handling of problems with large deformations is allowed by using the SPH method [33].
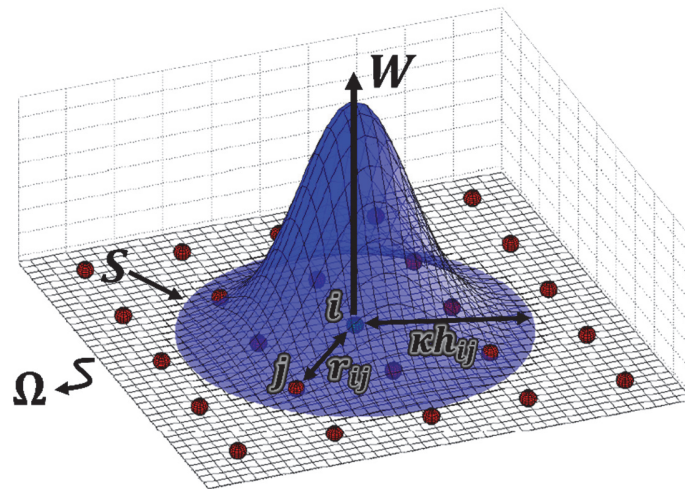

Figure 5: SPH particles in a 2D problem domain.

A numerical technique, namely FEM-coupled to-SPH, was developed, inspired by [25], to take advantage of both the FEM and the SPH methods. The Lagrangian meshed elements were eroded after reaching a certain criterion by using this technique, and they were adaptively transformed to SPH particles that inherit identical mechanical properties with the failed elements. The implementation of this technique in LS-DYNA was carried out by calling the keyword called ADAPTIVE_SOLID_TO_SPH. However, since many of the material keywords available in the LS-DYNA material library, i.e. the ones used in this study (KCC), do not have any internal eroding algorithm, an external eroding algorithm is required to be implemented in conjunction with this keyword. The element erosion of the models of this article was obtained by using MAT_ADD_EROSION and specifying a certain value for the maximum shear strain (EPSSH). Therefore, each hexahedral solid element who meets this criterion will be eroded, and then by defining the two input parameters of ADAPTIVE_SOLID_TO_SPH keyword as ICPL=1 and IOPT=1, the software automatically replaces those eroded elements with a certain number of SPH particles. The number of particles can be controlled by the users, i.e. it can be 1, 8 or 27 in case of hexahedral elements (see Fig. 6). Within this study, the failed solid elements were converted into one SPH particle to keep the time consumption cost low.
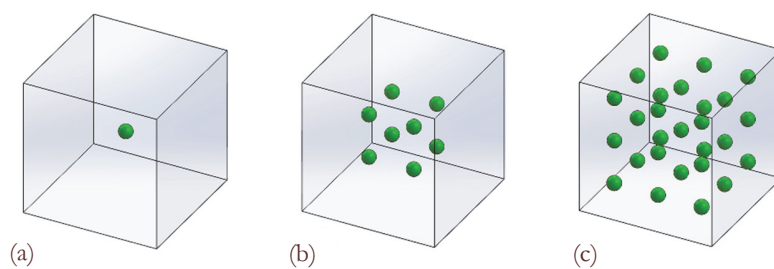

Figure 6: Transformed SPH particles from a hexahedral 3D solid element.

This method can be implemented in ABAQUS by choosing the option "conversion to particles" from "element type" panel at the mesh module. Unlike the LS-DYNA, an external eroding algorithm in never required since the elements which meet a user-specified criterion are automatically transformed to a certain number (from 1 up to 343) of SPH particles. The maximum principle strain is considered as the conversion criterion for all the models developed by ABAQUS in this study.

Karagozian and Case Concrete (KCC) model
The studies on the nonlinear concrete material models that were implemented by the Lagrangian finite element code DYNA3D at 1992 (reported in [34]), showed that the material model 16 (concrete/geological material) presented appropriate and attractive features. To overcome the shortcomings of this material model, Malvar et al. developed another

model within 1994 to 2000 [26-29], known as the "Karagozian and Case Concrete (KCC or K&C)" model, by applying several significant enhancements to the material model 16.

The Karagozian and Case concrete model, implemented in LS-DYNA, consists of three-invariant failure surface formulation, i.e. $f = f(I_1, J_2, J_3)$, where I_1 is the first principal invariant of the Cauchy stress, J_2 and J_3 are the second and third principal invariants of the deviatoric part of the Cauchy stress, respectively. It is more convenient to use a cylindrical set of coordinate system for the cohesive frictional material since the principal stresses can be immediately recast into this format as Eq. (4). The formulation of KCC model is explained by means of this cylindrical coordinate system as a clearer way of guidance for readers.

$$\begin{bmatrix} \sigma_1 \\ \sigma_2 \\ \sigma_3 \end{bmatrix} = \frac{1}{\sqrt{3}} \begin{bmatrix} \xi \\ \xi \\ \xi \end{bmatrix} + \sqrt{\frac{2}{3}} \cdot \rho \begin{bmatrix} \cos\theta \\ \cos(\theta - 2\pi/3) \\ \cos(\theta + 2\pi/3) \end{bmatrix} \qquad (4)$$

where, the ξ, ρ and θ are the Haigh-Westergaard coordinates defined as Eq. (5).

$$\begin{cases} \xi = \dfrac{1}{\sqrt{3}} I_1 = \sqrt{3} p \\[2mm] \rho = \sqrt{2 J_2} = \sqrt{2/3}\, \sigma_{eq} \qquad\qquad [\sigma_{eq} = q] \\[2mm] \cos(3\theta) = \left(\dfrac{r}{q}\right)^3 = \dfrac{3\sqrt{3}}{2} \dfrac{J_3}{J_2^{3/2}} \qquad [r = 3\left(\dfrac{1}{2} J_3\right)^{1/3}] \end{cases} \qquad (5)$$

The failure function of the KCC material model can be derived by Eq. (6) in terms of the Haigh-Westergaard stress invariants.

$$f = f(\xi, \rho, \theta) = f_c(\xi, \rho) \cdot \hat{r}[\Psi(p), \theta] \qquad (6)$$

where, $f_c(\xi, \rho)$ corresponds with the failure surface in the triaxial compression state of stress, when the Lode angle θ is equal to $60°$, and the non-dimensional function $\hat{r}[\Psi(p), \theta]$ is the ratio between the current radius of the failure surface and the compressive meridian. The Eq. (6) is discussed in detail below.

The Karagozian and Case concrete model takes advantage of the three-fixed independent failure surfaces in the compressive meridian ($\xi - \rho$ plane), which correspond to the yield, the ultimate and the residual strength of the material. Hence, the function $f_c(\xi, \rho)$ is defined for each one of these failure surfaces separately by Eqs. (7), (8) and (9).

$$(\rho)_y = \sqrt{2/3}\, a_{0_y} + \frac{\sqrt{2}\, \xi'}{3 a_{1_y} + \sqrt{3}\, a_{2_y} \xi'} \qquad [\xi' = \xi - \frac{0.55}{\sqrt{2}} (\rho)_m; (\rho)_m = 0.45 (\rho)_y] \qquad (7)$$

$$(\rho)_m = \sqrt{2/3}\, a_0 + \frac{\sqrt{2}\, \xi}{3 a_1 + \sqrt{3}\, a_2 \xi} \qquad (8)$$

$$(\rho)_r = \frac{\sqrt{2}\, \xi}{\sqrt{3}\, a_{1_f} + a_{2_f} \xi} \qquad (9)$$

The stress invariants for an axisymmetric loading condition, when $\sigma_1 = \sigma_a$ is the axial stress and $\sigma_2 = \sigma_3 = \sigma_l$ are the lateral stresses, can be re-written as Eq. (10).

$$\begin{cases} \xi = I_1/\sqrt{3} = (\sigma_a + 2\sigma_l)/\sqrt{3} \\ \rho = \sqrt{2J_2} = \sqrt{2/3}(\sigma_a - \sigma_l) \\ \cos(3\theta) = 1 \end{cases} \tag{10}$$

Therefore, the equations of the three-failure surfaces for the axisymmetric state of stress can be written as the Eqs. (11), (12) and (13).

$$(\Delta\sigma)_y = a_{0_y} + \frac{p'}{a_{1_y} + a_{2_y} p'} \qquad [p' = p - \frac{0.55}{3}(\Delta\sigma)_m; \ (\Delta\sigma)_m = 0.45(\Delta\sigma)_y] \tag{11}$$

$$(\Delta\sigma)_m = a_0 + \frac{p}{a_1 + a_2 p} \tag{12}$$

$$(\Delta\sigma)_r = \frac{p}{a_{1_f} + a_{2_f} p} \tag{13}$$

where, the a_i - parameters are the user-defined input parameters to define the failure surfaces in the compressive meridian. These parameters can be calibrated based on the experimental data of the triaxial compression test by means of a curve-fitting approach, e.g. a genetic algorithm. The parameter p is the pressure (positive in compression) or the mean stress equal to $(\sigma_1 + \sigma_2 + \sigma_3)/3$. The meridian plane defined by means of the above-mentioned equations is shown schematically in Fig. 7.
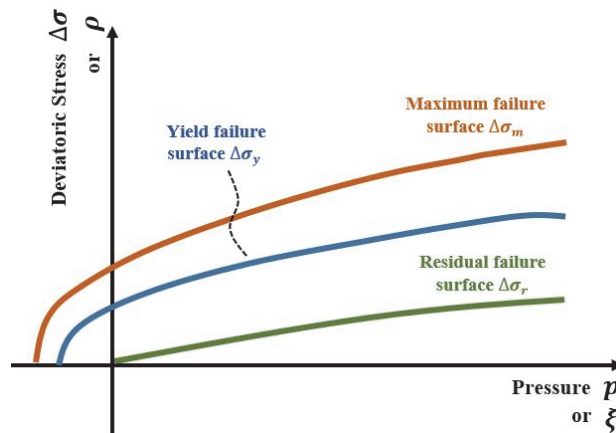

Figure 7: Schematic representation of the KCC failure surfaces in the compressive meridian.

As written in the Eq. (6), the KCC material model considers the effect of the third invariant, i.e. the Lode angle θ, by means of the function $\hat{r}[\Psi(p),\theta]$. This function was derived from the Eq. (14), which is the shape of the failure criterion in the deviatoric plane, proposed by Willam and Warnke [35].

$$r(\theta) = \frac{2r_c(r_c^2 - r_t^2)\cos\theta + r_c(2r_t - r_c)\sqrt{4(r_c^2 - r_t^2)\cos^2\theta + 5r_t^2 - 4r_t r_c}}{4(r_c^2 - r_t^2)\cos^2\theta + (2r_t - r_c)^2} \tag{14}$$

where, $r(\theta)$ determines the distance of the failure surface at the deviatoric section by considering the effect of the Lode angle θ. The parameters r_c and r_t express the distances of failure surfaces from the hydrostatic axis at the compressive and

tensile meridian, respectively. The deviatoric plane of a Willam-Warnke failure model is indicated in Fig. 8. In this figure, the TXC, TXE and SHR stand for triaxial compression, triaxial tension and pure shear respectively.
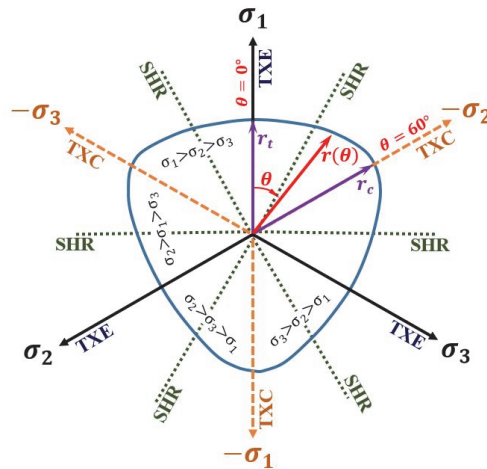

Figure 8: Deviatoric section proposed by Willam-Warnke model

The $\hat{r}[\Psi(p),\theta]$, which is the ratio between the current radius of the failure surface $r(\theta)$ and the distance of the failure surfaces from the hydrostatic axis at the compressive meridian r_c, is computed by means of the Eq. (15). This equation was obtained by dividing both sides of Eq. (14) by r_c. In order to present the term $\Psi(p)$, which is a strength index of brittle material related to the confining pressure that a material is subjected to it and equal to $\Delta\sigma_t/\Delta\sigma_c$ (in KCC model also equal to r_t/r_c), both the numerator and the denominator of the right-hand side of equation are divided by r_c^2.

$$\hat{r}[\Psi(p),\theta] = \frac{r(\theta)}{r_c} = \frac{2(1-\Psi^2)\cos\theta + (2\Psi-1)\sqrt{4(1-\Psi^2)\cos^2\theta + 5\Psi^2 - 4\Psi}}{4(1-\Psi^2)\cos^2\theta + (1-2\Psi)^2} \tag{15}$$

The fact that $\hat{r}$ is just a function of $\Psi(p)$ and θ, and the lode angle can be determined based on the loading conditions, implies the role of $\Psi(p)$ for computational purposes. It means that the implementation of the three invariant failure surfaces is completed by means of this parameter $\Psi(p)$. This parameter generally depends on the hydrostatic stress and can be obtained empirically. Malvar et al. in [28] defined this parameter as a linear piecewise function on the full range of pressure according to Eq. (16).

$$\Psi(p) = \begin{cases} \dfrac{1}{2}, & -f_t \leq p \leq 0 \\ 1/2 + 3f_t/2f_c', & p = f_c'/3 \\ \dfrac{\alpha f_c'}{a_0 + \dfrac{2\alpha f_c'/3}{a_1 + 2a_2\alpha f_c'/3}}, & p = 2\alpha f_c'/3 \\ 0.753, & p = 3f_c' \\ 1, & p \geq 8.45 f_c' \end{cases} \tag{16}$$

Where f_c' is the unconfined compression strength, f_t is the principal tensile strength and α is an experimental parameter related to the biaxial compression test. According to the Eq. (16), $\Psi(p)$ varies from 1/2 to 1, which is in accordance with the experimental data previously obtained. It also indicates that $p = 8.45 f_c'$ is the transition point in which the compression meridian is equal to tension one, and accordingly from this point onwards, there is a circular failure surface on the deviatoric

plan section. Moreover, it considers a value equal to 1⁄2 for the negative range of pressures. It is worth mentioning that this function was implemented in LS-DYNA and no input is required of the users.

One of the most noteworthy features of the KCC model is decoupling the shear and compaction behaviour of the materials, which means that this model treats the deviatoric and volumetric responses separately. The deviatoric response is characterized by the migration of the current stress state between the fixed failure surfaces, while the response to pressure is defined by an equation of state as a function of volumetric strain increments.

The damage accumulation of the KCC model, and accordingly the current failure surfaces are expressed schematically in Fig. 9. As can be seen in Fig. 9a, the state of stress is determined by a linear interpolation between the three failure surfaces. The stress-strain diagram corresponding to the unconfined compression test is indicated in Fig. 9c, which is determined by association of a damage accumulation function (shown in Fig. 9b. The response of the material to the initial loading, phase I in Fig. 9c, is considered as a linear elastic deformation before reaching point 1 in Fig. 9a. The current failure surface $\Delta\sigma_{c.f.}$ is therefore the same as the yield strength level $\Delta\sigma_y$ at this range. A hardening plasticity response occurs after yielding and before reaching the maximum strength. The KCC material model determines the current state of stress at this range (between point 1 and point 2) according to Eq. (17).

$$\Delta\sigma_{c.f.} = \eta(\Delta\sigma_m - \Delta\sigma_y) + \Delta\sigma_y \tag{17}$$

Based on the level of confining pressure, a softening response occurs after reaching the maximum strength and before obtaining a residual strength. The current state of stress corresponds to this area (between point 2 and point 3) is derived according to Eq. (18).

$$\Delta\sigma_{c.f.} = \eta(\Delta\sigma_m - \Delta\sigma_r) + \Delta\sigma_r \tag{18}$$

where η is the KCC damage parameter used to determine the relative location of the current failure surface, which is a function of another parameter, called the accumulated effective plastic strain λ.
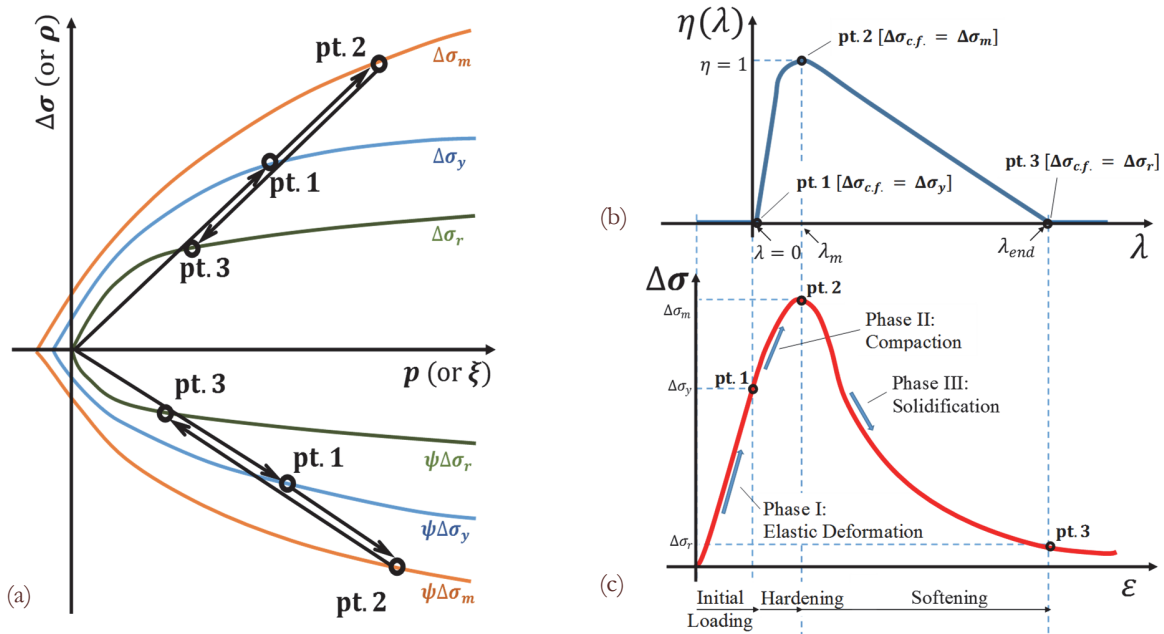

Figure 9: a) the linear interpolation between failure surfaces, b) the damage function, c) unconfined compression stress-strain diagram.

As can be seen in Fig. 9b, the damage function is described so that initially and prior to the occurrence of any plasticity responses, the value of η is set to zero. It increases up to unity at a user-defined value λ_m, corresponding to point 2, where the maximum failure surface has been reached. The KCC model considers the hardening plasticity by means of this linear-piecewise function of η - λ. After point 2, where the softening takes place, η decreases to zero at λ_{end} corresponding to point

3, which indicates that after this point the current failure surface $\Delta\sigma_{c.f.}$ is the same as the residual strength level $\Delta\sigma_r$. This tabulated damage function of the KCC model can be determined by up to 13 pairs of η - λ parameters. The variation of η and λ is summarized in Tab. 2.

η	λ	Current failure surface position
$0 \leq \eta < 1$	$0 \leq \lambda < \lambda_m$	$\Delta\sigma_y \leq \Delta\sigma_{c.f.} < \Delta\sigma_m$
$\eta = 1$	$\lambda = \lambda_m$	$\Delta\sigma_{c.f.} = \Delta\sigma_m$
$1 \geq \eta > 0$	$\lambda_m \leq \lambda \leq \lambda_{end}$	$\Delta\sigma_m \leq \Delta\sigma_{c.f.} \leq \Delta\sigma_r$

Table 2: The KCC damage evaluation parameters.

This material model implements shear damage accumulation by including the rate effect enhancement and different scenarios in tension and compression as Eq. (19).

$$d\lambda = \begin{cases} d\lambda = \dfrac{\overline{d\varepsilon^p}}{[1+(s_\lambda/100)(r_f-1)](1+p/r_f f_t)^{b_1}}, & 0 \leq p \\[4mm] d\lambda = \dfrac{\overline{d\varepsilon^p}}{[1+(s_\lambda/100)(r_f-1)](1+p/r_f f_t)^{b_2}}, & p \leq 0 \ (uniaxial) \\[6mm] \Delta\lambda = b_3 \, f_d \, k_d (\varepsilon_v - \varepsilon_v^{yield}), & p \leq 0 \ (triaxial) \end{cases} \tag{19}$$

where, $p = (\sigma_1 + \sigma_2 + \sigma_3)/3$ and f_t are pressure (positive in compression) and maximum tensile strength, respectively. The $\overline{d\varepsilon^p}$ is, the effective plastic strain increment equal to $\sqrt{(2/3) de_{ij}^p de_{ij}^p}$ (and $e_{ij}^p = \varepsilon_{ij}^p - (1/3)\delta_{ij}\varepsilon_{kk}^p$ is the deviatoric part of strain). The parameter s_λ expresses the strain rate effect user-defined factor; if it is equal to 0, the strain-rate effects is toggled off, while if it is equal to 100, the strain-rate effects is included. The parameter r_f is the dynamic increase factor that accounts for the strain rate effects. Parameters b_1 and b_2 govern the softening in compression and uniaxial tensile strain, respectively, whereas, b_3, affects the triaxial tensile strain softening. These b-parameters can be determined by iteration until the value of the fracture energy, G_f, converges for a specified characteristic length, which is associated with the localization width (i.e. the width of the localization path transverse to the crack advance).

To describe the rock compaction behaviour in LS-DYNA, this *MAT_072R3 is used in conjunction with an Equation-of-State (EOS), namely *EOS_TABULATED_COMPACTION. This EOS provides a function of the current and previous volumetric strain ε_v for the current element pressure p. The stress tensor can be computed as being a point on a movable surface by means of known pressure. This surface can be a yield or a failure surface. This function should be specified by users as a series of ε_v, p, K sets, where K is the bulk modulus correspondent to the different $p - \varepsilon_v$ pairs [20]. These series can be generated internally by the automatic input generation mode of this material model. In case of an essential change of stiffness of a material, the linear bulk modulus which is defined as the 20, can be adjusted.

$$K = -\frac{p_2 - p_1}{\varepsilon_{v2} - \varepsilon_{v1}} \tag{20}$$

The most significant improvement provided by the third release of this material model is the automatic input parameter generation capability, based solely on the unconfined compression strength [29]. This makes the use of the KCC model easier and accessible to most users, since there is no need to carry out extensive material characterization tests. The KCC model was originally developed to analyze the mechanical behaviour of concrete, and although the response of sandstone is expected to be similar to concrete, the results of the automatic input generation mode are only a rough estimation for

sandstones. However, this automatic method was used initially within this study due to the overwhelming number of input parameters which are difficult to obtain from current resources. Apart from the numerical results which are obtained directly from the automatic mode, LS-DYNA also generates all the input parameters automatically and writes them into the "MESSAG" file. Therefore, some of these parameters (i.e. the b-parameters) can be used in addition to the other parameters provided for the users by other resources.

Previous studies [36, 37] showed that the mechanical behaviour of Berea sandstone is expected to be very similar to the Pietra Serena. Since the experimental data related to the triaxial compression test of Pietra Serena sandstone is not available (which is required for calibrating the a_i - parameters), it was decided to use the experimental data of the Berea sandstone for the calibration the KCC material model. The initial input parameters used for the automatic mode were obtained from [38] and reported in Tab. 3.

Density, RO [ton/mm³]	Poisson ratio, PR	UCS, A0 [MPa]	NOUT	RSIZE	UCF
2.00e-9	0.34	-62.00	2.00	0.03937	145.00

Table 3: The experimental data of Berea sandstone provided for the automatic mode.

The parameters RSIZE and UCF are unit conversion factors and the NOUT is called the "output selector for effective plastic strain". According to [39], when NOUT=2, the quantity labelled as "plastic strain" by LS-PrePost is actually the quantity that describes the "scaled damage measure, δ" which varies from zero to two. When the amount of δ is still lower than one, the elements of the part modelled by the KCC, don't reach the yield limit. When this amount is equal to two, the corresponding elements meet the residual failure level. Only at the automatic mode of MAT_072R3 keyword (when a maximum of six parameters are defined) the A0 parameter must be defined as a negative number to represent the unconfined compression strength. For instance, the -62 in Tab. 3, means the UCS is considered equal to 62 [MPa].

Tab. 4 expresses the results obtained from the automatic input generation mode of MAT_072R3, after performing the initial simulation, which were also used at the full input calibration mode.

B1	B2	B3	ω	S_λ	E_{drop}	LOC-WIDTH
1.1	1.35	1.15	0.5	100	1.00	1.35

Table 4: The results obtained from the automatic input generation mode of MAT_072R3.

Where, the parameters ω, E_{drop} and LOC-WIDTH are the frictional dilatancy, post peak dilatancy and three times of the maximum aggregate diameter, respectively. Almost all of the EOS tabular data obtained from the automatic input generation mode, were also used for the full input calibration mode. Only the "Pressure02" parameter from EOS keyword was changed to 26.1 [MPa] to reach the same bulk modulus (and accordingly the elastic behaviour) as the Berea sandstone. The tensile strength parameter was investigated in another recent study by the same authors [37] where the Brazilian tensile test was performed on Pietra Serena and the tensile strength was determined as 5.81 [MPa].

The pairs of η - λ parameters were changed to the values reported in [40]. A new set of a_i - parameters were computed by the least square curve fitting method from the experimental triaxial compression tests [20]. These experimental data which were performed at four different confining pressure levels are reported in [41]. The a_i - parameters are reported in Tab. 5 (note that the A0 parameter here is a positive value).

A0 [MPa]	A1 [MPa]	A2	A0Y [MPa]	A1Y [MPa]	A2Y	A1F [MPa]	A2F
34.458	0.65629	0.00097	21.621	1.11569	0.00251	0.7563	0.00097

Table 5: The a_i-parameters experimental of Berea sandstone provided for the full input mode.

Extended (Linear) Drucker-Prager model

This is an advanced material model implemented by ABAQUS, which is based on the conventional Drucker-Prager constitutive law. There are three forms of the extended Drucker-Prager material model developed in ABAQUS which are the linear, the hyperbolic and the general exponential forms [30]. Within this research work, the linear form of this model was investigated. The linear Drucker-Prager (LDP) model consists of a pressure-dependent three-invariant failure surface which obtains the opportunity of having the non-circular yield surface (unlike the conventional Drucker-Prager) in the

deviatoric plane. This model also takes advantage of the associated inelastic flow and hardening (or softening) rules, and different dilation and friction angles. The general form of the failure surface in the Haigh-Westergaard coordinate system is given by Eq. (21).

$$f = f(\xi, \rho, \theta) = t(\rho, \theta) - \frac{\tan\beta}{\sqrt{3}}\xi - d(\epsilon_p) \tag{21}$$

The effect of the Lode angle θ is considered by $t(\rho, \theta)$ according to the Eq. (22).

$$t(\rho, \theta) = \sqrt{\frac{3}{8}}\left[(1+\frac{1}{K}) - (1-\frac{1}{K})\cdot\cos 3\theta\right]\rho \tag{22}$$

where the material parameter K is defined as the ratio of yield stresses at triaxial tension to triaxial compression, which means it controls the shape of the linear Drucker-Prager yield function at the deviatoric plane. As can be seen in Fig. 10b, if $K=1.0$, a circular failure function presents in the deviatoric plane, which is the same as the conventional Drucker-Prager. It is proved that in order to verify the convexity of the yield function, the value of parameter K should be in the range of 0.778 to 1.0. By means of an approach to match the parameters of the Mohr-Coulomb and linear Drucker-Prager (for materials with low friction angles), K can be defined according to Eq. (23).

$$K = \frac{3 - \sin\varphi}{3 + \sin\varphi} \tag{23}$$

where, φ is the internal friction angle used in Mohr-Coulomb model. The parameter β is commonly termed as the friction angle (in case of dealing with the Drucker-Prager theory), which can be computed as the slope of the yield function in the t-p meridian plane (see Fig. 10a. By a similar computing approach for K, it is possible to derive β according to Eq. (24).

$$\beta = \arctan(\frac{6\sin\varphi}{3 - \sin\varphi}) \tag{24}$$

It is worth mentioning that both the parameter can be defined in ABAQUS as a function of temperature and other field variables. However, they are considered as constant variables in this study because of the negligible effect of the other fields. The parameter d, called the cohesion of the material (in case of dealing with the Drucker-Prager model), is defined automatically by ABAQUS according to Eq. (25).

$$d(\epsilon_p) = (1 - \frac{1}{3}\tan\beta)\sigma_{uc}\epsilon_p \tag{25}$$

where, σ_{uc} is the unconfined (uniaxial) compression stress. An isotropic hardening is implemented for this model in ABAQUS by a sub-option called "Drucker-Prager Hardening" at the property module. Therefore, the tabular data from the compression post-yield stress-strain diagram can be used to define σ_{uc} (and accordingly d) as a function of the absolute plastic strain ϵ_p. The plastic flow of the linear Drucker-Prager is considered by means of a flow potential function G_{LDP} given by Eq. (26).

$$G_{LDP} = t - p\tan\psi \tag{26}$$

The parameter ψ, called dilation angle, specifies the direction of the plastic strain flow. As can be seen in Fig. 10a, the plastic flow is associative if $\psi = \beta$, otherwise it is non-associative. The parameters to identify the material model are reported in Tab. 6. The software automatically computes the cohesion by giving the yield stress in compression as a function of the plastic strain allowing the isotropic hardening of the yield function.
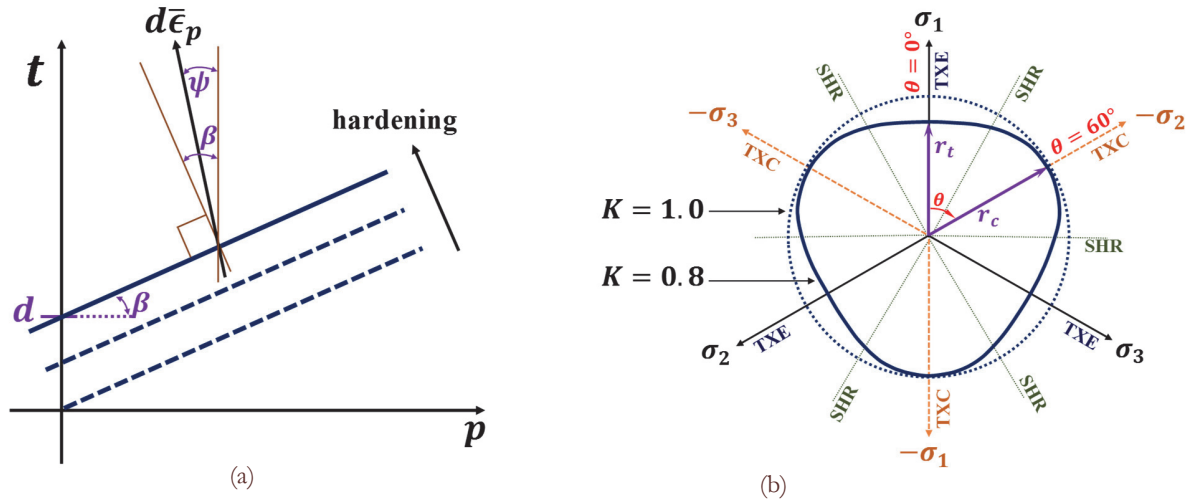
Figure 10: The Linear Drucker-Prager criterion; (a) t-p plane, (b) deviatoric plane.

E [MPa]	PR	β [°]	K [-]	ψ [°]
15374	0.28	65.38	0.778	16.35

Table 6: The Drucker-Prager plasticity parameters.

In this study, the failure criterion is intended as a yield surface, i.e. when Eq. (21) is satisfied, plastic flow occurs. Hardening of the yield function follows until the maximum strength is reached, afterwards failure is modeled by softening. Hardening (intended as hardening followed by softening) of the yield function (see Fig. 11) is described by the equation proposed by Lubliner et al., [42] for concrete as defined in Eq. (27).

$$\sigma = f_0 \cdot [(1+a) \cdot \exp(-b \cdot \epsilon_p) - a \cdot \exp(-2b \cdot \epsilon_p)] \tag{27}$$

Eq. (27) expresses the flow stress σ in a uniaxial test as a function of the axial plastic strain ϵ_p. The elastic properties are taken from [36]. The Mohr-Coulomb friction angle is obtained through the procedure described in [43] using the properties reported in Tab. 7. To assure convexity of the yield function, the value of the flow-stress ratio is limited by a minimum value of 0.778. Since the obtained value is lower, the minimum value allowable is used instead resulting in the criterion obtained not being equivalent to the starting Mohr-Coulomb criterion but being its best approximation [30].

UCS, f_m [MPa]	Tensile splitting strength [MPa]	Yield stress, f_0 [MPa]	$\overline{\epsilon_p}$
67.99	5.66	53.79	0.00057

Table 7. The experimental data of the Pietra-Serena sandstone.

A good approximation of the dilation angle for rock showing brittle behavior is equal to 1/4 times the friction angle [44]. In Tab. 7, the parameters to define the curve of Eq. (27) are reported. The parameters *a* and *b*, which are obtained using Eqs. (28) and (29), are determined equal to 2.68 and 665.32, respectively. It is worth mentioning that the plastic strain at Eq. (29) (to define the parameter *b*) is determined when the derivative of Eq. (27) is equal to zero. This plastic strain corresponds to the experimental data at which the maximum stress is reached.

$$a = \left(\frac{f_m}{f_0}\right) - 1 + 2\sqrt{\left(\frac{f_m}{f_0}\right)^2 - \left(\frac{f_m}{f_0}\right)} \tag{28}$$

$$b = -\left(\overline{\epsilon_p} \Big/ \ln\frac{1+a}{a}\right) \tag{29}$$

Simulation of the four-point bending test

Replication of the Flexural test was obtained by means of two numerical models that consists of rollers, compressive platens, steel blocks and the specimen. Due to the high computing time required for the KCC, and by help of the symmetric nature of the test, only one-quarter of the test was modelled in LS-DYNA (see Fig. 12a). Since the ghost particle methods (which is explained below) is not yet available in ABAQUS, the numerical model replicated in this software consists of the full model (see Fig. 12b). In all the models, the conversion to SPH particles is only considered for the rock specimen. The axes of rollers are fixed in the XY plane, while the displacement-controlled compressive loading is applied by the upper platens. The lower platens are limited to zero degree of freedom to represent the bed of the testing machine. The mechanical properties of these components are reported in Tab. 8.
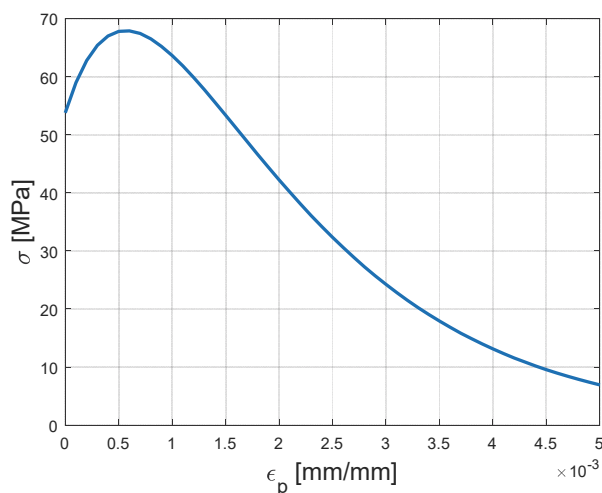

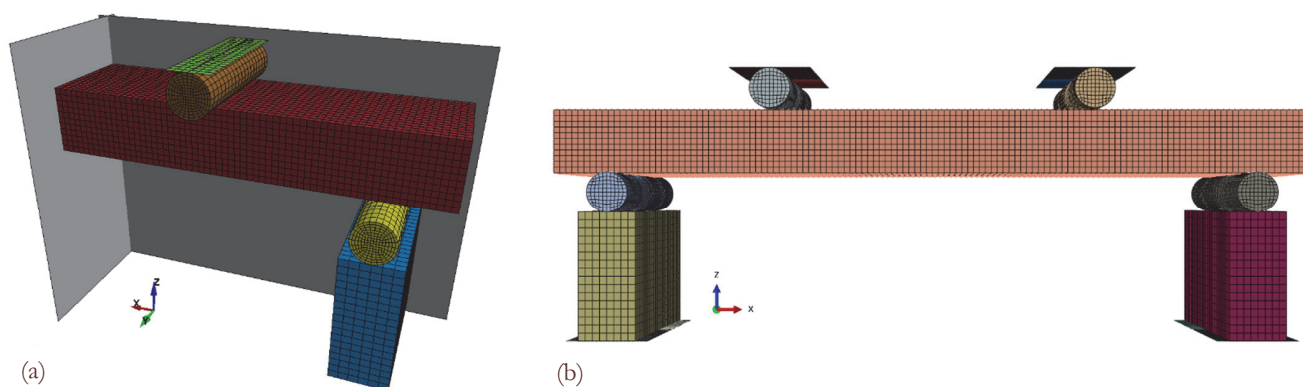Figure 11: The post-yield stress-strain diagram in compression.

(a)　　　　　　　　　　　　　　(b)

Figure 12: The numerical models of Flexural test replicated in; (a) LS-DYNA, (b) ABAQUS.

	Rollers	Platens	Steel blocks
Section	Solid	Shell	Solid
Material model	Elastic	Rigid	Elastic
Density [ton/mm³]	7.85 e-9	7.85 e-9	7.85 e-9
Elastic modulus [MPa]	1.9 e5	2.1 e5	2.1 e5
Poisson ratio	0.3	0.3	0.3

Table 8: The mechanical properties of the rollers, platens and steel blocks.

The hexagonal constant stress elements are used for all the solid parts. The automatic penalty-based formulation contacts are considered for all the components and the static friction coefficient is set to 0.4. In the LS-DYNA model, instead of applying single point constraints to the SPH particles, which can lead to inaccurate results and numerical instabilities, specific boundary conditions at the symmetry planes were imposed [39]. The BOUNDARY_SPH_SYMMETRY_PLANE keyword creates automatically an imaginary plane which reflects the forces of a set of ghost particles to the particles in the model. Although these ghost particles have identical properties as the real ones, they do not physically exist and simply contribute to the particle approximation [21].
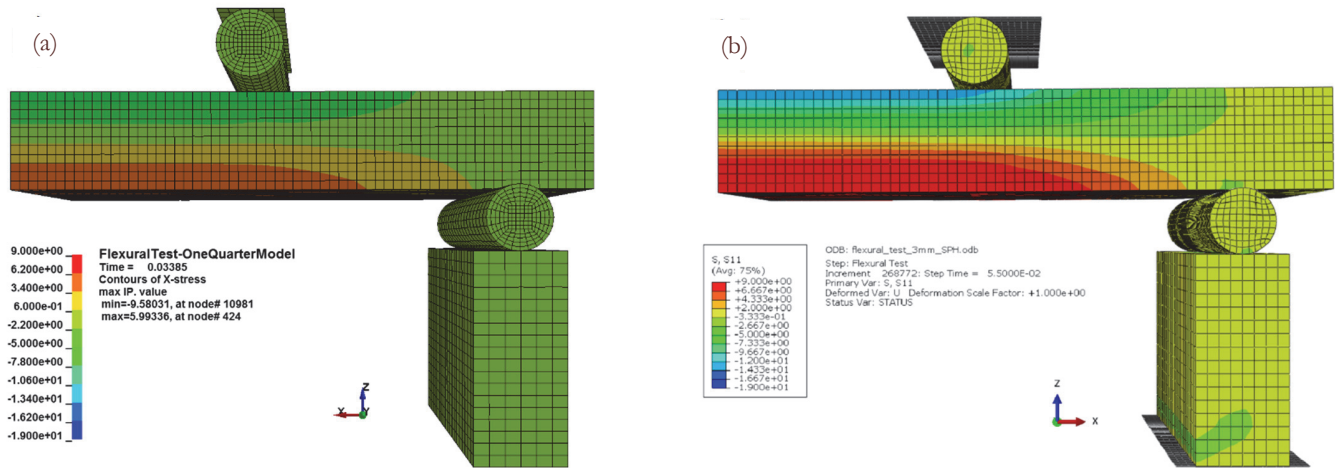

Figure 13: Distribution of numerical stresses in the X direction (along the length); (a) KCC model; (b) LDP model.

The maximum principal strain is considered as the eroding criteria for FEM to SPH particles conversion for all the numerical simulations. The numerical results of KCC and LDP models in terms of stress distribution along length are shown in Fig. 13a and b, respectively.

Fig. 13 represents the distribution of the X stress (along the length of specimen) one time step before failure. The tensile and the compressive stresses at both numerical models are present in the element below and above the neutral axis, respectively. However, the amount of maximum stresses in the two models are different. This issue is discussed in next chapter by comparison of the numerical results with the experimental ones.

COMPARISON OF THE NUMERICAL RESULTS WITH EXPERIMENTAL DATA

The load-displacement diagrams of the numerical models; developed by the KCC (both the automatic input generation mode and the calibrated mode) and the LDP material models are compared to the experimental results according to Fig. 14 and Tab. 9. There is a row in Tab. 9, labeled as "95% CI" of experimental average value, that was also reported in Tab. 1. As previous described there is a probability of 95% that the average value of a set of populations lie inside this interval. Therefore, they can be considered a reasonable description of the physical phenomena thus suitable for comparing the numerical results.

The KCC material model shows the best response compared to the others, since the reported values of all three parameters, i.e. Maximum load, Maximum displacement and Flexural strength, lie within the 95% Confidence Interval of the average value. As expected, the results obtained by the automatic input mode of the KCC model are not in good agreement with the experimental data. This issue is more critical in the displacement level, and the flexural strength is very close to the minimum value reported as 95% Confidence Interval.

LDP predicts the flexural strength as 16.25 MPa which is far from the reported 95% Confidence Interval (with an overestimation of about 80% respect to the experimental average value). Therefore, it is not reliable to model the mechanical behaviour of Pietra Serena in case of a significant tensile stress is present. Indeed, the Drucker-Prager criterion is well suitable to model the linear dependence of the material strength with p. The material behaviour of rocks, for negative values of p, deviates from linearity and the material failure points lie below the Drucker-Prager failure line leading to the overestimation of the flexural strength of the material. The numerical results obtained by the full calibrated mode of KCC, on the other hand, show significant agreement with the experimental data. By recalling the fact that this material model is

calibrated based on the Berea sandstone (experimental data of the triaxial compression test), two main conclusions can be drawn. Apart from the authors' hypothesis of a similar mechanical response of Pietra Serena and Berea sandstone, the efficiency of the KCC model for numerical modelling of rock materials, and in particular sandstones, has been evaluated here.

	Maximum Load [kN]	Maximum Displacement [mm]	Flexural Strength [MPa]
KCC Automatic	3.10	0.137	7.13
KCC Calibrated	3.54	0.337	8.14
LDP	7.07	0.891	16.25
"95% CI" of experimental data	[3.1433 - 4.5275]	[0.36737 - 0.74223]	[7.2530 - 10.7140]

Table 9: The numerical results of the flexural test, and the "95% CI" with respect to the average experimental data.

Fig. 15 indicates the comparison of the numerical results and the experimental test after failure. The contour plots represented in Fig. 15a and b represent the "scaled damage measure, δ" and the maximum principal plastic strain at failure, respectively. As can be seen, the SPH particles formed at the instant of failure express the crack patterns observed during the experimental test (see Fig. 15c).
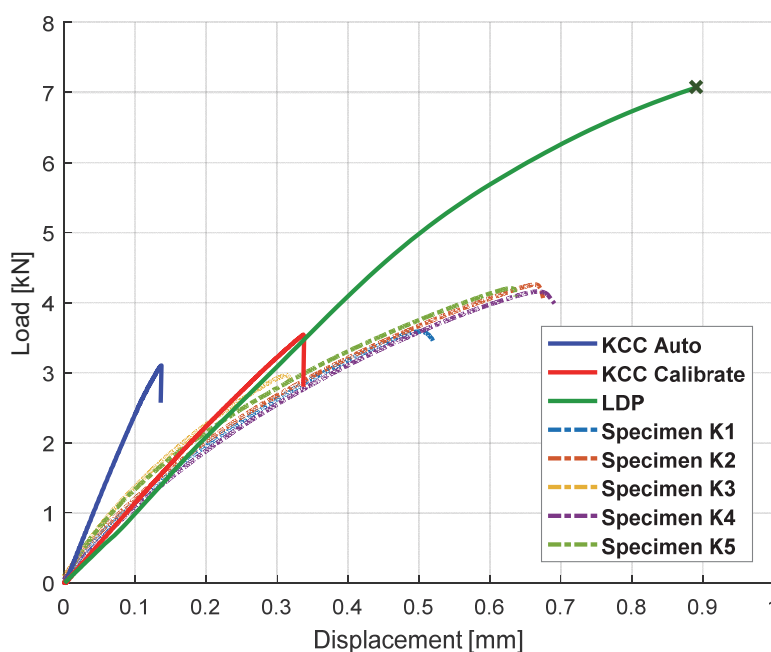

Figure 14: The load-displacement diagram; the numerical results compared to the experimental ones.

CONCLUSION

The Four-Point Bending tests were performed based on the protocols of the ASTM standard. The average experimental flexural strength of Pietra Serena was measured as 8.98 MPa and Pietra Serena and Berea Sandstone show similar mechanical properties. The numerical simulations using the FEM-coupled to-SPH method were implemented in conjunction with the KCC and LDP material models. The KCC model showed a significant improvement when the material input parameters were calibrated and directly inserted into the material keyword, instead of the automatic input generator mode. While the LDP material model showed some limitation in analyses of the state of stress in which tensile behaviour is present. The specifications of the KCC calibrated material model are summarized in Tab. 10.
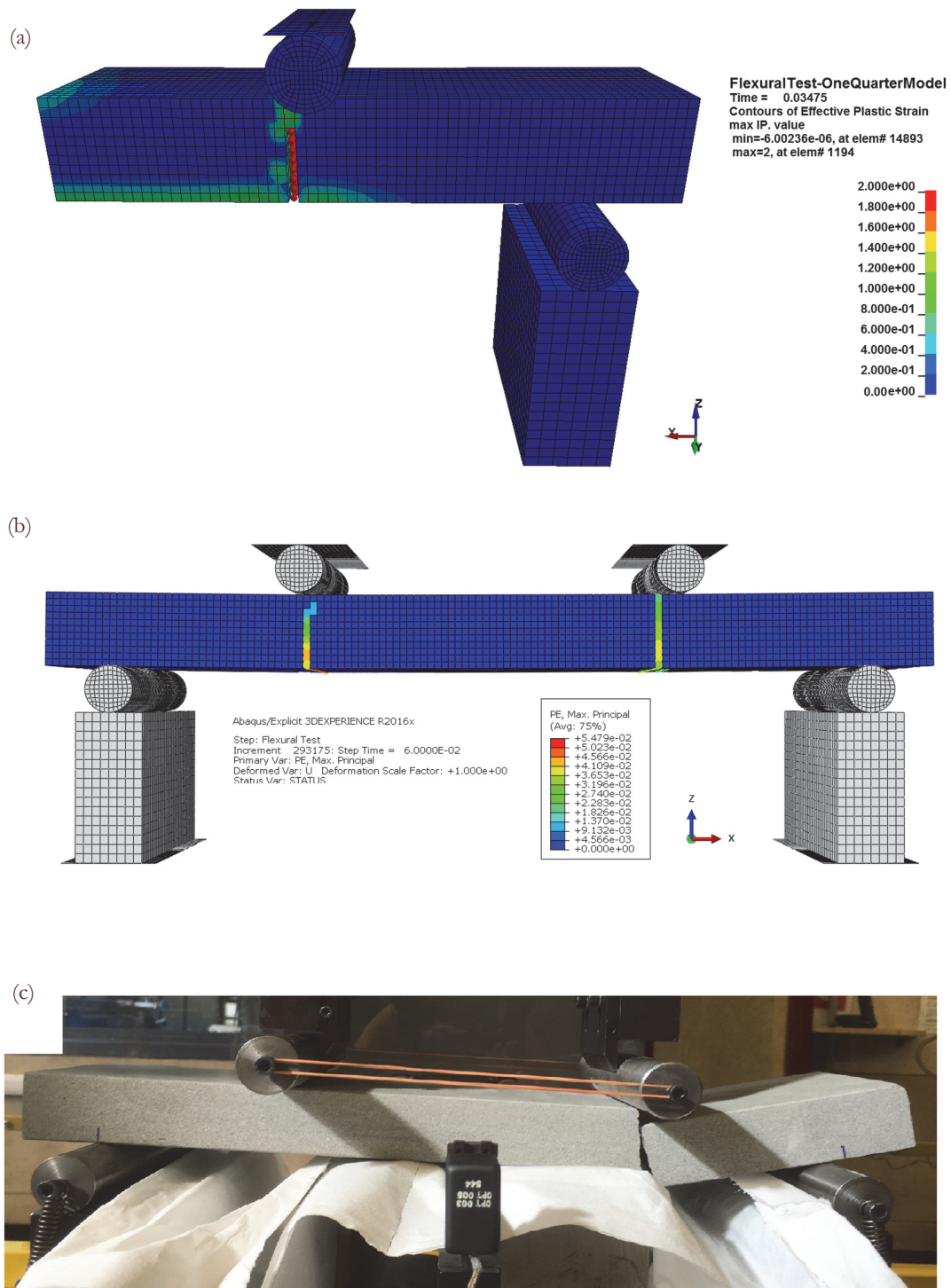
(a)

(b)

(c)

Figure 15: The comparison of the numerical results and the experimental test after failure.

The flexural strength obtained by the numerical models developed by the LDP and the KCC automatic input mode lie significantly out of the 95% Confidence Intervals of the average value, as predicted from statistical elaboration of experimental data, while, this issue is solved by implementing the calibrated input mode of KCC.

The coupling of SPH and FEM was proved to be a reliable method to simulate crack generation. This method was shown to be an effective solution to simulate several rock mechanics applications that deal with large deformations, e.g. penetration, drilling, perforation, etc.

The numerical results are expected to be improved by a direct material identification based on the Pietra Serena, i.e. the triaxial compression and isotropic compression tests.

Density, RO [ton/mm³]			Poisson ratio, PR		NOUT	RSIZE	UCF
2.00e-9			0.34		2.00	0.03937	145.00

B1	B2	B3	ω	S_λ	E_{drop}	LOC-WIDTH	
1.1	1.35	1.15	0.5	100	1.00	1.35	

A0 [MPa]	A1 [MPa]	A2	A0Y [MPa]	A1Y [MPa]	A2Y	A1F [MPa]	A2F
34.458	0.65629	0.00097	21.621	1.11569	0.00251	0.7563	0.00097

Table 10: The specifications of the full input mode of the KCC material model implemented for Berea sandstone.

REFERENCES

[1] Brook, N., The measurement and estimation of basic rock strength, Comprehensive rock engineering, 3 (1993) 41-66.

[2] Hudson, J.A., Crouch, S.L., Fairhurst, C., Soft, stiff and servo-controlled testing machines: a review with reference to rock failure, Eng Geol, 6 (1972) 155-189.

[3] Gopalaratnam, V., Shah, S.P., Softening response of plain concrete in direct tension. Journal Proceedings, (1985) 310-323.

[4] Biolzi, L., Cattaneo, S., Rosati, G., Flexural/tensile strength ratio in rock-like materials, Rock Mech Rock Eng, 34 (2001) 217-233.

[5] Jaeger, J.C., Cook, N.G.W., Fundam Rock Mech, (1979).

[6] Cattaneo, S., Rosati, G., Effect of different boundary conditions in direct tensile tests: experimental results, Magazine of Concrete Research, 51 (1999) 365-374.

[7] Bažant, Z.P., Kazemi, M.T., Size effect in fracture of ceramics and its use to determine fracture energy and effective process zone length, Journal of the American Ceramic Society, 73 (1990) 1841-1853.

[8] Labuz, J., Biolzi, L., Class I vs class II stability: a demonstration of size effect. International Journal of Rock Mechanics and Mining Sciences & Geomechanics Abstracts: Elsevier, (1991) 199-205.

[9] Biolzi, L., Labuz, J., Global instability and bifurcation in beams composed of rock-like materials, International journal of solids and structures, 30 (1993) 359-370.

[10] Price, N., A study of the time-strain behaviour of coal-measure rocks. International Journal of Rock Mechanics and Mining Sciences & Geomechanics Abstracts: Elsevier, (1964) 277-303.

[11] Laws, V., Derivation of the tensile stress-strain curve from bending data, Journal of Materials Science, 16 (1981) 1299-1304.

[12] Mayville, R., Finnie I. Uniaxial stress-strain curves from a bending test, Experimental Mechanics, 22 (1982) 197-201.

[13] Pepper, J.F., Geology of the Bedford Shale and Berea Sandstone in the Appalachian Basin: A Study of the Stratigraphy, Sedimentation and Paleogeography of Rocks of Bedford and Berea Age in Ohio and Adjacent States: US Government Printing Office, (1954).

[14] Hamilton, W.B., Tectonics of the Indonesian region: US Govt. Print. Off., (1979).

[15] Khodja, M., Canselier, J.P., Khodja-Saber, M., Cohaut, N., Drilling fluid technology: performances and environmental considerations, INTECH Open Access Publisher, (2010).

[16] Coli, M., Livi, E., Tanini, C., Pietra Serena in Fiesole, Part I: A historic stone resource in need of cultural and cognitive recovery, J of Min Sci, (2002).

[17] Coli, M., Livi, E., Tanini, C., Pietra Serena in Fiesole, Part II: Geological setting and quarrying, J of Min Sci, 39 (2003).

[18] Coli, M., Livi, E., Tanini, C., Pietra Serena mining in Fiesole, Part III: Structural-mechanical characterization and mining, J Min Sci, 42 (2006) 74-84.

[19] Kochavi, E., Kivity, Y., Anteby, I., Sadot, O., Ben-Dor, G., Numerical model of composite concrete walls, Proceedings of the 9th Biennial ASME Conference on Engineering Systems Design & Analysis, ESDA2008 (2008).

[20] Jaime, M.C., Numerical modeling of rock cutting and its associated fragmentation process using the finite element method: University of Pittsburgh, (2011).

[21] Anghileri, M., Castelletti, M.L., Francesconi, E., Milanese, A., Pittofrati, M., Rigid body water impact–experimental tests and numerical simulations using the SPH method, Int J Impact Eng, 38 (2011) 141-151.

[22] Wu, Y., Crawford, J.E., Numerical Modeling of Concrete Using a Partially Associative Plasticity Model, J Eng Mech, 141 (2015) 04015051.

[23] Zhao, H., Zhang, C., Cao, W.g., Zhao, M.h., Statistical meso-damage model for quasi-brittle rocks to account for damage tolerance principle, Environ Earth Sci, 75 (2016) 1-12.

[24] Olleak, A.A., El-Hofy, H.A., SPH Modelling of Cutting Forces while Turning of Ti6Al4V Alloy, (2015).

[25] Bresciani, L., Manes, A., Romano, T., Iavarone, P., Giglio, M., Numerical modelling to reproduce fragmentation of a tungsten heavy alloy projectile impacting a ceramic tile: Adaptive solid mesh to the SPH technique and the cohesive law, Int J Impact Eng, 87 (2016) 3-13.

[26] Malvar, L.J., Crawford, J.E., Wesevich, J.W., Simons, D., A new concrete material model for DYNA3D, A New Concrete Material Model for DYNA3D, (1994).

[27] Malvar, L.J., Crawford, J., Wesevich, J., Simons, D., A new concrete material model for DYNA3D-Release II: shear dilation and directional rate enhancements, A Report to Defense Nuclear Agency under Contract No DNA001-91-C-0059, (1996).

[28] Malvar, L.J., Crawford, J.E., Wesevich, J.W., Simons, D.A., plasticity concrete material model for DYNA3D, Int J Impact Eng, 19 (1997) 847-873.

[29] Malvar, L.J., Crawford, J.E., Morrill, K.B., K&C concrete material model release III-automated generation of material model input. K&C Technical Report TR-99-24-B12000.

[30] Manual ASUs. Dassault Systemes Simulia Corp, Providence, RI, (2009).

[31] ASTM. Test Method for Flexural Strength of Dimension Stone. C 880-98. West Conshohocken, PA: ASTM International, (1998).

[32] Meda, A., Tensile behaviour in natural building stone: Serena sandstone, Materials and Structures, 36 (2003) 553-559.

[33] Liu, M., Liu, G., Smoothed particle hydrodynamics (SPH): an overview and recent developments, Archives of computational methods in engineering, 17 (2010) 25-76.

[34] Shugar, T., Holland, T., Malvar, L.J., Applications of finite element technology to reinforced concrete explosives containment structures. DTIC Document, (1992).

[35] Willam, K., Warnke, E., Constitutive model for the triaxial behavior of concrete, Proceedings, international association for bridge and structural engineering: ISMES, Bergamo, Italy, (1975) 1-30.

[36] Mardalizad, A., Manes, A., Giglio, M., An investigation in constitutive models for damage simulation of rock material. AIAS, Associazione Italiana Per L'analisi Delle Sollecitazioni, Università Degli Studi Di Trieste, Italy (2016).

[37] Mardalizad, A., Manes, A., Giglio, M., Investigating the tensile fracture behavior of a middle strength rock: experimental tests and numerical models, 14th International Conference on Fracture (ICF14), Rhodes, Greece (2017).

[38] ASTM. Standard Test Method for Compressive Strength and Elastic Moduli of Intact Rock Core Specimens under Varying States of Stress and Temperatures, D 7012-04. West Conshohocken, PA: ASTM International, (2004).

[39] Hallquist, J.O., LS-DYNA® Keyword User's Manual: Volumes I, II, and III LSDYNA R7. 1, Livermore Software Technology Corporation, Livermore (LSTC), Livermore, California, 1265 (2014).

[40] Markovich, N., Kochavi, E., Ben-Dor, G., An improved calibration of the concrete damage model, Finite Elements Anal Des, 47 (2011) 1280-1290.

[41] Ding, J., Experimental Study on Rock Deformation and Permeability Variation: Texas A&M University, (2013).

[42] Lubliner, J., Oliver, J., Oller, S., Onate, E., A plastic-damage model for concrete, International Journal of solids and structures, 25 (1989) 299-326.

[43] Sivakugan, N., Das, B., Lovisa, J., Patra, C., Determination of c and φ of rocks from indirect tensile strength and uniaxial compression tests, International Journal of Geotechnical Engineering, 8 (2014) 59-65.

[44] Hoek, E., Brown, E.T., Practical estimates of rock mass strength, Int J Rock Mech Min Sci, 34 (1997) 1165-1186.